

Research papers

Experimental characterisation and numerical modelling of a structured thermocline energy storage system under different operating conditions

Jordi Vera^a, Christian Odenthal^b, Oriol Sanmartí^a, Carlos D. Pérez-Segarra^{a,*}

^a *Universitat Politècnica de Catalunya - BarcelonaTech (UPC), Heat and Mass Transfer Technological Center (CTTC), Carrer de Colom 11, 08222 Terrassa, Barcelona, Spain*

^b *German Aerospace Center (DLR), Institute of Engineering Thermodynamics, LinderHöhe, Building 26, 51147, Köln, Germany*

ARTICLE INFO

Keywords:

Pilot-scale experimental unit
Structured thermocline
Thermal energy storage
Ceramic filler material
Numerical analysis

ABSTRACT

This paper presents the first pilot-scale experimental demonstration of a molten salt structured thermocline thermal energy storage system. The study combines both experimental and numerical approaches to assess the performance and feasibility of this novel configuration. The experimental campaign was conducted at the thermal energy storage in molten salts (TESIS) facility at the DLR, where the storage tank consists of three vertically stacked baskets filled with clinker bricks. A series of dynamic cycling tests were carried out to evaluate the system's response under realistic operating conditions. In parallel, an unsteady and one-dimensional model was developed to simulate the thermal behaviour of the structured thermocline consisting of different layers of material. The model was validated against experimental data, showing good agreement across various charging and discharging cycles with different cutoff temperatures and mass flow rates. The experiments showed that allowed cut-off temperature affected the thermocline thickness much more than the mass flow rate. Moreover, the experiments successfully demonstrated the feasibility of the thermocline storage concept with refractory bricks, as it was possible to establish a stable thermocline for multiple cycles, confirming the potential of structured configurations for large-scale thermal storage applications.

1. Introduction

Thermal energy storage (TES) systems are increasingly recognised as a key technology to address the intermittent nature of renewable energy sources, particularly in concentrated solar power (CSP) plants [1,2]. These systems allow for the efficient storage and dispatch of thermal energy, enabling solar power plants to operate effectively beyond sunlight hours [3,4].

Thermal energy storage systems based on thermocline configurations have emerged as a promising alternative to traditional two-tank systems [5]. These systems operate by establishing a temperature gradient (or thermocline) within a single tank, thus reducing the need for separate hot and cold reservoirs. When combined with low-cost filler materials or encapsulated phase change materials (PCMs) [6], thermocline TES systems can significantly reduce investment costs while maintaining good thermal performance [7].

While packed beds composed of natural stones or gravel have been extensively studied and offer a straightforward and inexpensive

solution, they present limitations in terms of homogeneity, pressure drop, reproducibility of thermophysical properties, and thermal ratcheting [8]. These issues may reduce thermal efficiency and make system design and scalability more challenging. In contrast, structured packed beds—sembled from well-defined ceramic or refractory bricks—allow for greater control over material properties, geometric arrangement, and flow distribution [9]. This improved control facilitates a more predictable and stable thermocline formation, especially under the dynamic conditions encountered in real CSP operation. For these reasons, structured thermocline systems are being increasingly investigated as a viable alternative that combines the economic advantages of packed beds with improved thermal management and design flexibility [10,11].

Several experimental studies have investigated the performance of thermocline TES systems using various filler materials and configurations. One of the earliest and most influential works was conducted by Pacheco et al. [12], who demonstrated the viability of using natural rock and sand as low-cost filler materials in a pilot-scale molten salt thermocline tank that measured approximately 6.1 m in height and 3.0 m in

* Corresponding author.

E-mail addresses: jordi.vera.fernandez@upc.edu (J. Vera), christian.odenthal@dlr.de (C. Odenthal), oriol.sanmarti@upc.edu (O. Sanmartí), cdavid.perez.segarra@upc.edu (C.D. Pérez-Segarra).

<https://doi.org/10.1016/j.est.2025.119463>

Received 13 August 2025; Received in revised form 14 October 2025; Accepted 8 November 2025

Available online 14 November 2025

2352-152X/© 2025 The Author(s). Published by Elsevier Ltd. This is an open access article under the CC BY license (<http://creativecommons.org/licenses/by/4.0/>).

diameter, operating between a hot temperature of approximately 395 °C and a cold temperature of around 290 °C. Their results showed that, despite some mixing at the thermocline interface, stable stratification could be achieved over multiple charge-discharge cycles. Subsequent studies expanded on this concept by exploring different rock types, tank geometries, and heat transfer fluids, often confirming the trade-off between cost-effectiveness and thermal efficiency.

A laboratory-scale thermocline TES experiment was conducted at the PROMES-CNRS laboratory by Hoffmann et al. [13]. The system consisted of a vertical tank with a total storage capacity of 8.3 kWh, filled with 325 kg of quartzite rocks (average particle diameter of 0.04 m) and thermal oil, yielding a porosity of 0.41. The active storage section measured 1.8 m in height and 0.4 m in diameter, with a discharge temperature set at 160 °C. At the same laboratory, 6 years later, Keilany et al. [14] combined sensible and latent heat storage materials encapsulated in tubes. The system employed synthetic oil as the heat transfer fluid (HTF), which was designed with a 4 m³ capacity, filled with 4.66 tons of alumina spheres. It also included a PCM layer of NaNO₃ encapsulated within stainless steel tubes, constituting 5.5 % of the tank's total volume. The tank operated at temperatures between 220 °C and 315 °C, with the NaNO₃ having a melting point of 306 °C.

Zanganeh et al. [15] initially conducted a high-temperature experiment utilising a truncated conical storage tank with a capacity of 6.5 MWh and a height of 4 m. The tank, packed with rocks, operated using air as HTF at temperatures reaching up to 650 °C. The system included extensive sensor arrays designed to thoroughly evaluate thermal gradients and quantify heat losses in a large-scale packed-bed configuration. Subsequently, three years later, Zanganeh et al. [16] integrated aluminium-silicon alloy (AlSi) as a PCM, encapsulated within tubes, into an experimental cylindrical storage tank measuring 1.68 m in height and 0.4 m in diameter, alongside rocks. Their results demonstrated that this combined latent and sensible heat storage configuration effectively stabilises the HTF outlet temperature near the melting point of the PCM when it remains partially molten.

Other authors, such as Advait et al. [17], have explored the potential of single-medium thermocline thermal energy storage systems, focusing on fluid-only configurations without solid filler material. Using a lab-scale setup with Hytherm-600 synthetic oil and an eccentrically mounted porous flow distributor, their study aimed to minimise mixing under near-adiabatic conditions, with precise temperature measurements along the tank height to evaluate thermocline stability and performance. Stathopoulos et al. [18] investigated a TES unit with a height of 2.39 m and a diameter of 1.1 m, employing magnetite ore as the filler material and Therminol SP as the HTF. Bruch et al. [19] studied a packed bed TES system filled with silica gravel and sand, with a height of 3 m and a diameter of 1 m, at the STONE laboratory. Their results showed that the thermocline evolution was highly controllable and reproducible during both charging and discharging processes.

Recent advancements, however, have shifted attention toward structured thermocline systems employing refractory materials, such as ceramic bricks, which promise higher thermal stability and lower costs for high-temperature applications. Although numerous experimental studies have extensively evaluated packed-bed thermal energy storage systems filled with traditional filler materials like rocks, sand, and gravel, including some integrating PCMs, research utilising structured materials remains sparse. McGregor and Snyman [20] investigated the development of structured ceramic composite bricks for TES, demonstrating promising thermal and structural properties through material testing and numerical studies. However, their work remained limited to laboratory-scale assessments and theoretical modelling, without an experimental validation of the structured thermocline concept under realistic operating conditions. Coventry et al. [21] proposed and fabricated a bench-scale prototype of a packed-bed TES using MgO bricks and liquid sodium as heat transfer fluid, but the concept remained at the stage of laboratory preparation, with no performance data reported. Zunft et al. [22] experimentally validated a large-scale structured

storage subsystem at the Jülich Solar Power Tower, where ceramic regenerators operated with air as the heat transfer fluid demonstrated stable cycling and low heat losses. While this work constitutes one of the very few experimental demonstrations of structured TES, its regenerator configuration and gaseous HTF differ significantly from molten-salt thermocline tanks.

This gap, particularly evident for molten-salt systems, highlights the lack of comprehensive experimental data on structured fillers and underscores the need for detailed investigations into their cyclic performance and thermal behaviour. Such studies are essential to validate the feasibility of structured thermocline systems, identify potential advantages, and optimise their designs for effective integration into high-temperature TES applications. In this context, the present work delivers the first pilot-scale experimental validation of a molten-salt structured thermocline system. A combined experimental and numerical investigation of a structured thermocline thermal energy storage system using refractory bricks as filler material. The experimental campaign was carried out at the TESIS facility of the German Aerospace Centre (DLR), where a pilot-scale tank composed of three vertically stacked baskets filled with clinker bricks was tested. The top basket was modified to include two additional layers of ceramic bricks to assess the thermal behaviour of different materials. To complement the experimental work, an unsteady one-dimensional numerical model was developed to simulate the thermal dynamics of the system under various charging and discharging cycles. The model was validated against the experimental data, with particular attention to the influence of cutoff temperatures and dynamic boundary conditions, showing good agreement across various charging and discharging cycles. The results demonstrate the viability of structured thermocline storage with refractory materials, confirming that a stable thermocline can be maintained across multiple cycles and supporting the feasibility of this concept for large-scale thermal energy storage applications.

The paper is structured in the following way:

- Section 1 introduces the context and motivation for the study, reviewing relevant literature and highlighting the novelty of the structured thermocline approach.
- Section 2 presents the experimental setup developed at DLR, including a description of the TESIS test facility and the configuration of the structured thermocline with refractory bricks.
- Section 3 describes the mathematical model and numerical methodology, covering the governing equations, discretisation strategy, model validation, and numerical parameters.
- Section 4 discusses the results obtained from both the experiments and simulations, including charging, discharging, and cycling tests.
- Section 5 summarises the main conclusions and outlines the implications of the study for future research and industrial applications.

2. Experimental approach

This section provides a detailed description of the experimental setup and the properties of the materials used in the thermal energy storage system. First, the working principle of the test facility is outlined, along with a description of its key components and their operation. Then, the arrangement of the refractory bricks within the storage unit is described, followed by an analysis of their structural characteristics. Finally, the derivation of the bricks' thermophysical properties and storage volume is presented, which is essential for accurately modelling the system's thermal behaviour.

2.1. Description of the functionality of the test facility

Fig. 1 shows a simplified flow diagram of the TESIS:store system at DLR. Molten salt is stored at two different temperature levels inside two reservoir tanks. The hot reservoir tank (right) provides salt for charging the thermocline storage tank. For charging, hot salt is pumped into the

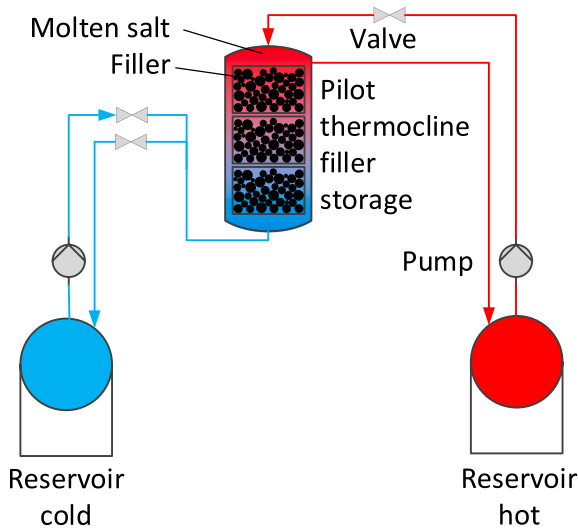


Fig. 1. Working principle of TESIS:store system.

thermocline tank from above, whilst cold salt leaves the tank at the bottom and flows into the cold reservoir tank from there. Fluid level inside the thermocline tank (centre) is maintained at a constant level just below the overflow line. During discharging, salt is pumped from the cold reservoir tank (left) into the thermocline tank from below. Hot salt flows back into the hot reservoir tank via the overflow in the upper part of the thermocline tank. To compensate for changes in the temperature of salt returning to the reservoir tanks, a cooler is integrated in the cold reservoir tank whilst an immersion heater is integrated in the hot reservoir tank.

To place the filler material into the storage tank, three metal baskets are used for this purpose, in which the fillers are placed. The metal baskets have a permeable floor made of perforated plates so that molten salt can flow through them. Between the baskets and the actual tank is a gap of 100 mm which fills up with molten salt during the filling process. The basic structure of the baskets is shown schematically in Fig. 2 (left) and a representation of the real system is provided in Fig. 3. The bottom basket rests on a circumferential support ring. To prevent the salt from flowing past the baskets, the top basket is topped with an attachment ring. This attachment ring has two purposes: First, the overflow line is

connected to the attachment ring via a flange, diverting the salt directly to the hot reservoir tank. Second, the attachment ring holds a flow distributor for the upper inlet to evenly spread inflowing hot salt during charging. The cold inlet at the bottom of the tank uses a baffle plate instead. The baskets themselves are sealed against each other by a large sealing ring made of glimmer. There are lifting lugs on the sides of the baskets, which are used to lift the baskets into the test facility using a crossbeam. For thermocouples, each basket has two feedthroughs on the sides of the baskets. To prevent flow through these feedthroughs, the thermocouples are run through a rectangular channel, which is welded to the baskets and ends above the liquid level.

The temperature measurement concept is illustrated in Fig. 2 as well:

- Detailed recording of the temperatures after each layer of bricks along the central axis in order to track the position of the thermocline, see Fig. 2 (right). In total 42 thermocouples inside filler plus 12 inside the sump and overflow region.
- Detailed measurement of the radial temperature distribution in three directions (f_0 , f_1 , f_2) at the top, mid and bottom region of each basket, to determine the homogeneity of the molten salt flowing in and out, see Fig. 2 (right). In total 9 layers with 9 thermocouples each.
- In general, a higher resolution near the wall is needed to better capture the influence of the wall on the temperature field (not shown).
- In total, 153 thermocouples were installed inside the tank.

2.2. Arrangement and structure of the refractory bricks

For testing, two types of refractory bricks were used. Due to limited availability, only the two topmost layers consisted of a specifically designed refractory brick delivered by the company Kraftblock GmbH. Mainly, commercially available refractory clinker bricks were used, but these did not have an optimised geometrical shape, see Fig. 4. The gaps between filler material and basket walls were filled with a packing of basalt chipping to minimise bypass streams. To achieve a slight spacing between each brick layer, a 2 mm thick layer of aviary stainless steel mesh was placed. This allows the flow to rearrange after each layer.

Due to the design of the baskets, there is a small void of 21 cm in height, which contains the support structure for the floors of the baskets. All geometric properties of the bricks and the storage volume can be seen in Fig. 4. From these dimensions, the geometric sizes summarised in

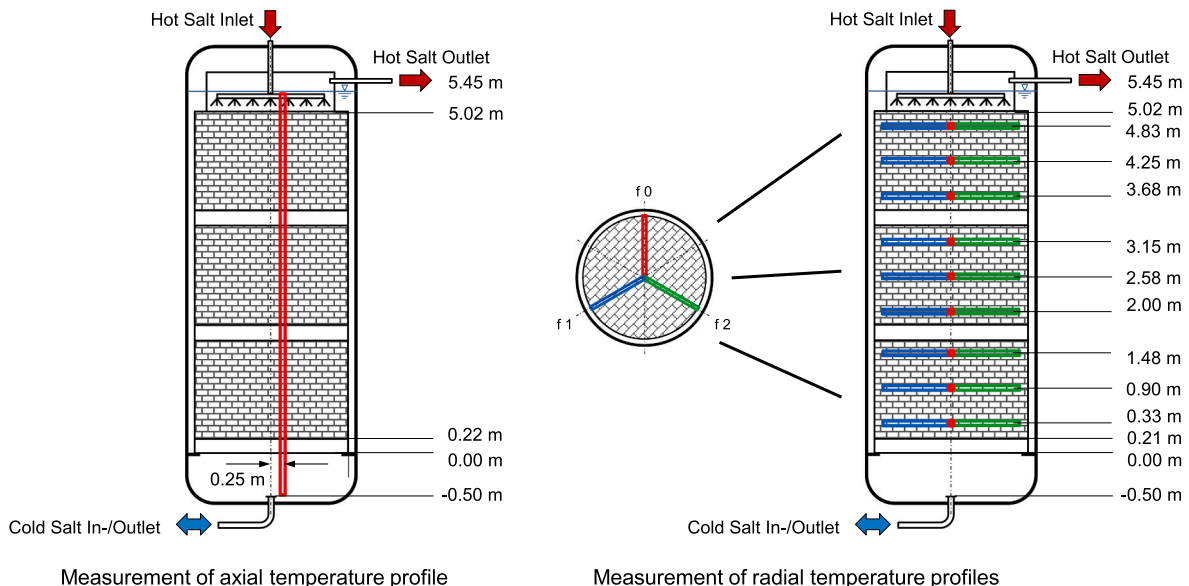


Fig. 2. Temperature measurement concept within the refractory bricks.



Fig. 3. Fully equipped baskets with clinker bricks (top left), top layer with Kraftblock bricks (top right) and detail view of the basalt chippings to fill the gap between filler and basket walls (bottom).

Table 1 were derived. These were calculated in five steps:

1. First, the geometric properties of the bricks were calculated, which were needed to obtain the hydraulic diameter from the following formula:

$$d_{hyd} = \frac{4A_0}{L_U} = \frac{4 \sum_{i=1}^n A_{0,i}}{n L_{U,i}}$$

Here, A_0 is the cross-section of the hole and L_U its circumference. As the holes are of different sizes, they must be averaged accordingly. When considering the bricks only, we get a void per brick of 29.3 % for Clinker and 10.6 % for Kraftblock bricks.

2. In the second step, the properties of the brick layers were calculated. The total area of all holes per layer was determined from the number of bricks and the cross-section of the baskets. The total number of bricks per layer is not an integer, as there are numerous cut bricks in the near-wall regions. Since the bricks have straight edges, whereas the baskets are round, there are gaps between the bricks and the baskets. These gaps are forming an additional cavity, which was filled with basalt chippings to avoid bypass flow. Also, the bricks cannot be packed perfectly, so there is always a small spacing between adjacent bricks. Thus, if the total number of bricks per layer is multiplied by the cross-sectional area of the holes and divided by the cross-sectional area of the baskets, one gets a smaller void ratio of 27.6 % for Clinker and 8.1 % for Kraftblock bricks. Therefore, this

proportion of cavity represents the lower limit for the achievable cavity.

3. In the third step, the properties of the bricks were evaluated. We use the number of bricks per basket multiplied by the weight of one brick to get the total weight of the bricks per basket. With the known density of the raw brick material, we can calculate the volume occupied by the raw brick material. For the top basket, different numerical values are obtained due to the mixing of different bricks, see Fig. 4.
4. In the fourth step, the mass and volume of the filler used to fill the gaps between bricks and baskets were calculated.
5. In the final fifth step, the volume of the filled area of the baskets was determined. The distance between the brick layers through the aviary wire mesh was also considered. This results in a higher void fraction.

The necessary simulation parameters, which were derived from the data in Table 1, are given in Table 2. Readings from the thermocouples at the top of the last basket ($z = 502$ cm) and the floor of the lowest basket ($z = 21$ cm) were used as the inlet temperature. Thus, the height of the investigated area is 4.805 m, and the inner diameter of the baskets, which is the relevant cross-section for the flow, is 1.98 m. The accuracy of the flow meter is assumed to be 5 % which has been derived from previous investigations. The thermocouples have a certain error of several Kelvin in absolute values; however, relatively to each other, the error can be assumed to be as low as 0.1 K.

Since the filler area is of variant composition, the model needs to consider different sections. The properties given in the table for the refractory bricks and the Kraftblock bricks have been derived from the previous Table 1. For the floors of the baskets, it is assumed that they are

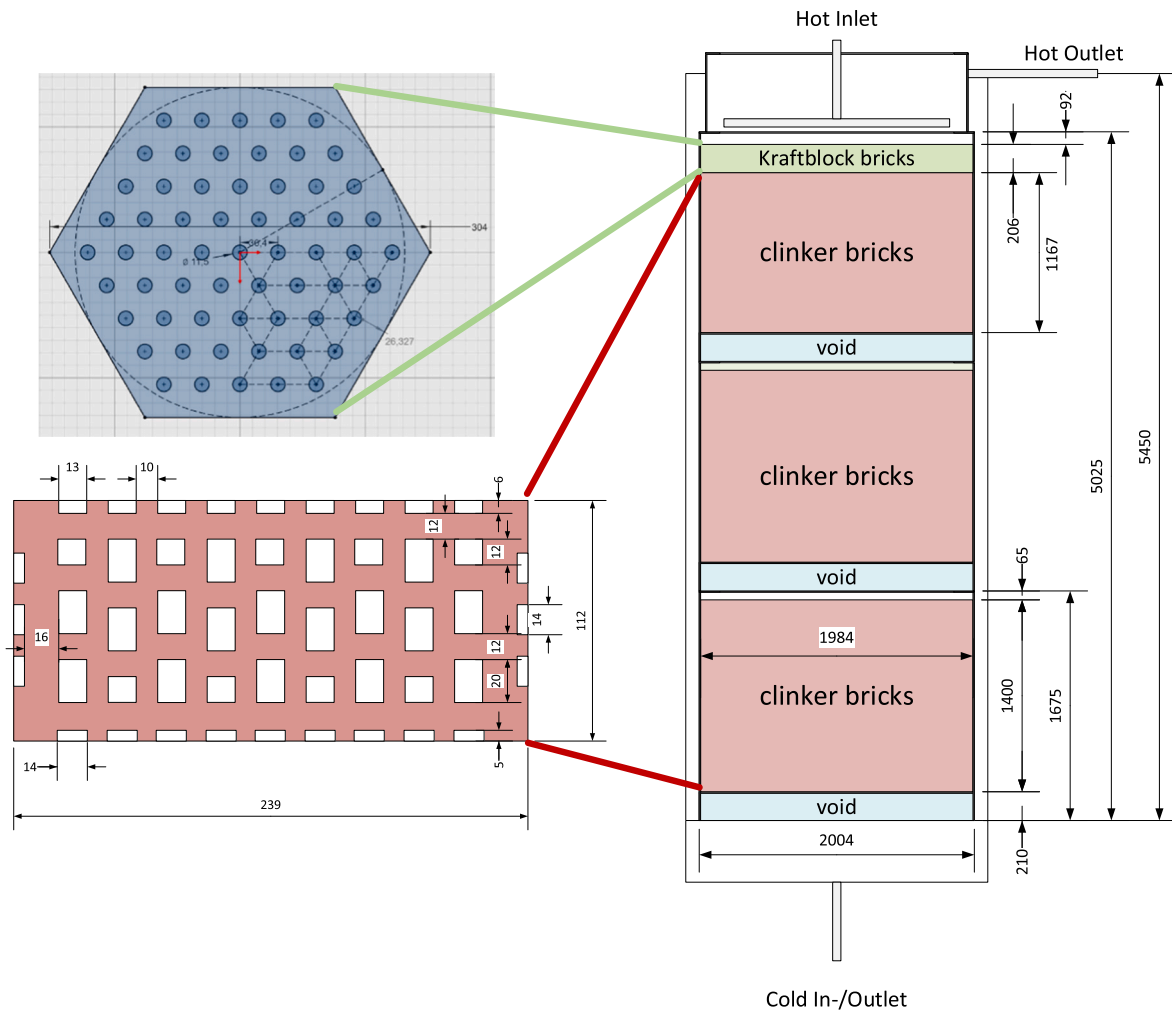


Fig. 4. Sketch of the filler material arrangement and dimensions of the TESIS:store test section.

filled with steel having a void fraction of 79.22 % and a hydraulic diameter of 11.5 mm. The void between the baskets is modelled as an area with no filler and 100 % void fraction.

3. Mathematical model and numerical methodology

This section presents the numerical model developed to simulate the thermal behaviour of the described structured thermozone system. It begins by introducing the governing equations and the numerical method used to solve them, followed by a description of the discretisation approach. The model's accuracy is assessed through verification and validation procedures. Finally, the numerical parameters applied in the simulations are detailed, including the layered configuration of the thermal storage unit and the thermophysical properties of the materials involved.

3.1. Governing equations and numerical method

Detailed modelling of each channel that forms the tank is very costly, computationally speaking. The proposed model considers the heat transferred from the fluid to the solid for all the channels, developing an unsteady and 1D approach, where only one node for the fluid and one node for the solid are used at any fluid cross-sectional area. With this equivalence, the model can be simplified, with each node having its own fluid temperature and solid temperature. Several assumptions are made to simplify the analysis:

- The radial heat conduction for the solid and fluid is neglected.
- The radial distribution of the flow is assumed to be uniform.
- The structured solid filler material is considered as a continuous and isotropic porous medium.
- The possible bypass between the solid filler material and the tank walls is neglected.
- The tank wall boundary condition is assumed to be adiabatic.

The study is conducted by solving the energy equations for the structured solid material in contact with a fluid. The physical properties are temperature-dependent. Similar models, like the continuous-solid-phase model, are usually used in the packed bed configuration [23,24]. The accumulation, convection and axial conduction terms are considered on the energy equation for the fluid and the solid.

HTF:

$$\epsilon \rho_f c_{p,f} \left(\frac{\partial T_f}{\partial t} + v_f \frac{\partial T_f}{\partial z} \right) = \hat{\alpha} (T_s - T_f) + \frac{\partial}{\partial z} \left(\lambda_f \frac{\partial T_f}{\partial z} \right) \quad (1)$$

Solid filler material:

$$(1 - \epsilon) \rho_s c_{p,s} \frac{\partial T_s}{\partial t} = \hat{\alpha} (T_f - T_s) + \frac{\partial}{\partial z} \left(\lambda_s \frac{\partial T_s}{\partial z} \right) - \dot{q}_{loss,s} \quad (2)$$

where ρ , λ and c_p are the density, thermal conductivity and specific heat, respectively, for the fluid (subscript f) and the solid (subscript s), ϵ the void fraction, v_f the axial velocity of the fluid flow, and $\dot{q}_{loss,s}$ represents the lateral heat losses per unit volume. The superficial heat transfer

Table 1
Measured and derived properties of the refractory brick material and the filler baskets of the TESIS facility.

Property	Clinker	Kraftblock	Unit
1. Geometric properties of the bricks			
Height of one brick	112	100	mm
Cross-sectional area of holes per brick	7836	6336	mm ²
Base cross-sectional area per brick	26,768	60,024	mm ²
Void fraction per brick	0.2927	0.1056	–
Number of big holes	18	61	–
Cross-sectional area of big holes	260	103.9	mm ²
Circumference of big holes	66	–	mm
Number of small holes	21	–	–
Cross-sectional area of small holes	156	–	mm ²
Circumference of small holes	50	–	mm
Hydraulic diameter	14.0	11.5	mm
2. Geometric properties of the brick layers			
Number of full bricks per layer	108.8	37 + 15 = 52	pcs
Cross-sectional area of the holes per layer	0.8526	0.249	m ²
Cross-sectional base area of all bricks per layer	2.9124	0.3295	m ²
Inner diameter of baskets	1984	–	mm
Inner cross-sectional area per basket	3.0915	–	m ²
Void fraction of the holes per layer	0.2758	0.0805	–
Thickness of aviary wire mesh	2	2	mm
Height of bricks without aviary wire mesh (per basket)	1.344 / 1.120	0.2	m
3. Brick properties			
Weight per brick	4422.2	12,400	g
Number of layers per basket 2 & 3 / basket 1	12 / 10	2	–
Mass of bricks basket 2 & 3 / basket 1	5773.6 / 4811.4	1289.6	kg
Density of pure material	2313	2350	kg/m ³
Pure material volume basket 2 & 3 / basket 1	2.496 / 2.080	0.549	m ³
4. Properties of the gap filler			
Mass of granular basalt per basket	222	–	kg
Pure density of basalt	2992	–	kg/m ³
Pure material volume	0.0742	–	m ³
5. Total properties			
Total height of brick packing with aviary wires	1.366 / 1.140	0.202	m
Total volume of brick material	2.570 / 2.142	0.561	m ³
Volume of packing area per basket	4.235 / 3.530	0.649	m ³
Void fraction	0.393	0.136	–
Total height of the basket	1.675	–	m
Height of the basket floor	0.21	–	m
Void left between packing and top of basket (baskets 2&3)	99	–	mm
Void left between packing and top of basket (basket 1)	123	–	mm

coefficient, α , is obtained from the volumetric one as $\alpha = \hat{\alpha}/a_s$, where a_s , is the heat transfer area of the bed per unit volume. The Nusselt number, based on the superficial heat transfer coefficient, was determined from an in-house CFD simulation [25], yielding a value of 4.36, consistent with the analytical solution for a constant heat flux boundary condition.

3.2. Discretisation details

The domain is discretised in a one-dimensional manner along the axial direction, resulting in a set of N control volumes, where nodes are

Table 2
Summary of derived properties for the computer simulations.

Boundary Conditions				
Upper / lower Temperature	560 / 290			°C
Mass flow	6 / 2			kg/s
Charging temperature	T at z = 502 cm (variable)			°C
Discharging temperature	T at z = 021 cm (variable)			°C
Allowed change of exit temperature	40 / 100			K
Heat transfer fluid (HTF)	Solar Salt			–
Filler material	Clinker Kraftblock A4 / B17 Basalt rocks (origin: D-Hühnerberg)			–
Measurement accuracy flow meter	± 5			%
Measurement accuracy of thermocouples	± 0.1			K
Properties of the storage volume				
Total Height	4.805			m
Inner diameter of baskets	1.98			m
	Refractory bricks	Kraftblock	Basket floor	Void
Number of sections	3	1	2	3
Height of the sections	1.366 / 1.140	0.202	0.210	0.099
				/ 0.123
Hydraulic diameter	14	11.5	0.1	–
Void fraction	0.3931	0.1356	0.7922	1

assigned at their centroid. The equations are numerically solved using a finite volume method (FVM), implemented in an in-house multilayered C++ software specifically designed for thermal energy storage systems. A first-order upwind differential scheme (UDS) is employed for the convective terms, and an implicit scheme is used for the time integration. For the charging process, the fluid is solved from top to bottom ($v_f < 0$). Using the UDS scheme, only the previously known fluid node is needed to solve the convective term. However, to resolve the diffusive term, information from the next node, which is unknown, is required. Therefore, a tri-diagonal matrix algorithm (TDMA) is used for the fluid and the solid. Additionally, a Gauss-Seidel iterative solver is used to solve the interaction between both domains. The same applies to the discharging process, but in the opposite direction ($v_f > 0$).

The energy equation for the fluid flow is discretised as follows:

$$\rho_{f,i} c_{p,f,i} \frac{T_{f,i} - T_{f,i}^0}{\Delta t} V_{f,i} + \dot{m}_i c_{p,f,i} (T_{f,n} - T_{f,s}) = \hat{\alpha}_i (T_{s,i} - T_{f,i}) V_i + \lambda_{f,n} \frac{T_{f,i+} - T_{f,i}}{\Delta z} S_{f,n} + \lambda_{f,s} \frac{T_{f,i} - T_{f,i-}}{\Delta z} S_{f,s} \quad (3)$$

The subscript i refers to the current control volume (CV). The subscripts $i+$ and $i-$ correspond to the adjacent CVs located in the upward (next) and downward (previous) directions, respectively. The second subscripts n and s refer to the north (upper) and south (lower) faces of the control volume, that is, the interfaces between nodes i and $i+$, and between nodes i and $i-$, respectively. The mass flow rate is given depending on whether the system is charging or discharging. During charging, the fluid moves from top to bottom, so the mass flow rate has a negative sign, with $T_{f,n}$ being $T_{f,i+}$ and $T_{f,s}$ being $T_{f,i}$ (UDS approach). In the discharging phase, the fluid flows from bottom to top, resulting in a positive mass flow rate, where $T_{f,s}$ is $T_{f,i-}$ and $T_{f,n}$ is $T_{f,i+}$.

For the solid, the energy equation includes a transient accumulation term, a volumetric heat exchange term with the fluid, and axial heat conduction through the solid, discretised as follows:

$$\rho_{s,i} c_{s,i} \frac{T_{s,i} - T_{s,i}^0}{\Delta t} V_{s,i} = \hat{\alpha}_i (T_{f,i} - T_{s,i}) V_i + \lambda_{s,n} \frac{T_{s,i+} - T_{s,i}}{\Delta z_{i+}} S_{s,n} + \lambda_{s,s} \frac{T_{f,i-} - T_{f,i}}{\Delta z_{i-}} S_{s,s} - \dot{q}_{loss,s} V_i \quad (4)$$

In this equation, the thermal conductivity at the north and south faces ($\lambda_{s,n}|\lambda_{s,s}$) is computed using the harmonic mean between adjacent control volumes, since the properties are temperature-dependent and the vertical direction includes different materials and regions. The fluid and solid volumes ($V_{f,i}, V_{s,i}$) are obtained considering the void fraction (ϵ) and the total volume of the CV (V_i). The surface areas at the north and south faces ($S_{f,n}, S_{s,s}$) represent the interface area between the current CV and its neighbour in the axial direction and are also adjusted according to the local void fraction. The axial spacing (Δz_i) corresponds to the distance between the centres of two adjacent control volumes.

3.3. Verification and validation

The code was carefully verified to ensure that the governing equations were correctly solved. Global and local mass, momentum, and energy balances were thoroughly checked. Similarly, local and global energy balances were performed to verify the accuracy of the thermal analysis within the solid domain. In all cases, a grid and time-step independent numerical study was conducted to confirm the robustness of the code, ensuring that the spatial and temporal discretisation were appropriate and sufficient for reliable results. For a detailed presentation of the numerical convergence study of mesh and time-step independence, readers are referred to [10] to avoid duplicating extensive verification data in the present work. In summary, the mesh and time-step sensitivity were evaluated by comparing the axial temperature profiles at a selected instant of the charging process. It was observed that reducing the averaged spatial discretisation below 0.01 m per node or the time step below 10 s did not lead to significant differences in the temperature distribution. Therefore, an averaged grid size of 0.01 m and a time-step of 10 s were adopted, which ensured accurate results while keeping the computational cost reasonable.

The mathematical formulation developed in this study has been validated against the experimental results by Odenthal et al. [26]. These experiments utilised the TESIS test facility at DLR, which corresponds to the same unit analysed in this paper, enabling a direct simulation of its thermocline storage structure. In that case, the storage tank was filled with 23 tons of basalt rock as the filler material, and solar salt was used as the heat transfer fluid. Fig. 5 shows a good agreement between the temperature profiles along the tank at different time intervals during the discharging process. It must be noted that during that time, there was a bypass-flow of approximately 20 % due to poor sealing of the baskets. Thus, the measured mass flow had to be reduced to obtain the actual

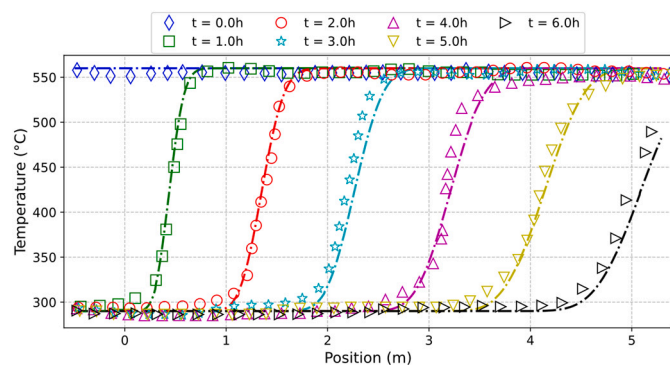


Fig. 5. Model validation against experiments at TESIS test facility using a packed bed as filler material with a mean mass flow rate of 1.5 kg/s [26]. Symbols correspond to the experimental measurements, while dashed lines represent the predictions of the developed numerical model.

mass flow through the centre of the baskets. The temperature profile is initialised at a hot temperature of 560 °C (cross symbol), representing the fully charged state of the thermal storage system. As the discharge process progresses, the temperature profile evolves at each hourly interval, with the thermocline gradually shifting from the inlet to the outlet. This is evidenced in the plot, where the steep temperature gradients move from left to right as the discharge continues from 0.0 h to 6.0 h. These comparisons indicate that the current model effectively captures the overall thermal behaviour of the system.

3.4. Numerical parameters

Regarding the current numerical simulation, it considers the structured thermocline with molten salt as the HTF. Table 3 shows the layer composition of the simulation for the structured thermocline at the TESIS facility. Based on the relation between the void fraction (ϵ), the diameter of the unit (D) and the diameter of the channels ($d_{channel}$), the total number of channels is estimated as $N_t = \epsilon D^2 / d_{channel}^2$. The table provides the type of layer and filler, where PB refers to Packed Bed and ST to Structured, along with the name of the filler material, the void fraction, the hydraulic diameter of the structured channels, the layer height (h_{bed}), and the number of control volumes (CVs) used in that layer.

The thermophysical properties for the molten salt are shown in Table 4. These properties were extracted from [27]. The thermophysical properties of the ceramic bricks (Clinker and KBB17/KBA4) are also shown in Table 4, and were obtained from own measurements considering that the porous material is fully saturated with molten salt.

4. Results

In this section, the numerical results obtained using the computational model are presented and compared with the experimental results from the TESIS facility. The analysis focuses on evaluating different charging and discharging cycles under various operating conditions, including mean mass flow rates of 2 kg/s and 6 kg/s, and cutoff temperature differences of 40 K and 100 K. Additionally, cycling tests are performed specifically at a mean mass flow rate of 6 kg/s, presenting results for the last discharge cycles with a 40 K cutoff temperature difference, as well as for the last cycle with a 100 K cutoff temperature difference.

4.1. Flow distribution and heat loss estimation

The focus in this publication lies on the thermocline behaviour, which was measured 25 cm shifted parallel to the centreline, to avoid influence of heat losses and influence of some flow patterns at the near wall regions. These assumptions shall be briefly discussed in this section.

To estimate the thermal losses of the system, dedicated standby tests were conducted. In these tests, the tank was fully charged and then left in standby conditions for approximately two days. The bulk temperature of the storage medium was measured at the beginning and end of this period using distributed thermocouples. From the measured temperature decrease and the known storage mass, the corresponding energy loss was calculated. Dividing this value by the standby duration provided the average heat loss rate of the system. When normalised by the nominal discharge power, the resulting heat losses correspond to approximately 0.35 %, confirming that thermal losses are negligible compared to the stored and discharged energy. Such low values of heat losses can be attributed to the fact that the baskets containing the filler material are placed inside a tank, which in turn is enclosed within an insulated external structure.

In terms of the flow distribution, the temperatures measured within a total of 9 layers at radial locations (3 layers per basket) were also analysed, see Fig. 2. Except for the measurements at the walls of the baskets,

Table 3
Layer composition of the structured thermocline at the TESIS facility considered at the numerical study.

	Layer 1	Layer 2	Layer 3	Layer 4	Layer 5	Layer 6	Layer 7	Layer 8	Layer 9
Layer Type	clinker refractory bricks	void above last row of clinker bricks	basket floor with steel structure	basket floor with steel structure	void above last row of clinker bricks	basket floor with steel structure	clinker refractory bricks	2 Kraftblock layers	void above Kraftblock bricks
Filler Type	Solid	Fluid	Solid	Solid	Fluid	Solid	Solid	Solid	Fluid
Filler	ST	-	PB	ST	-	PB	ST	KBA4	-
	Clinker	-	Steel	Clinker	-	Steel	Clinker	KBB17	-
Void fraction	0.3931	1	0.7922	0.3931	1	0.7922	0.3931	0.1356	1
$d_{channel}$ (m)	0.014	-	0.011	0.014	-	0.011	0.01	0.0115	-
h_{bed} (m)	1.366	0.099	0.21	1.366	0.099	0.21	1.14	0.202	0.123
CVs	136	10	21	136	10	21	11.4	20	12

the temperatures closely followed the temperatures along the centreline. This backs up the assumption that the flow is homogeneous within the bulk of the baskets and that heat losses in radial direction are negligible. However, uncertainties remain present in the near-wall regions of the baskets, which originate from (i) potential bypass flow between filler material and basket walls due to irregular brick cutting and settling of the basalt chipping filler (see section 2.2), and (ii) heat transfer from the baskets to the annular gap between baskets and tank walls as well as heat transfer through the stagnant molten salt in the annular gap and its thermal inertia (see section 2.1).

4.2. Charging tests

All the computational simulations follow the same procedure. The temperature profile is initialised using the experimental data at $t = 0$ to ensure consistency with the observed conditions. The inlet temperature is given as a boundary condition and is updated every 5 s to reflect real-time variations in the system. Similarly, the instantaneous inlet mass flow rate is also prescribed as a boundary condition, and it is updated every 5 s ensuring that the simulation accurately captures the dynamic behaviour of the system. Fig. 6 presents the dynamic boundary conditions for the inlet temperature (in this case, the hot temperature) and mass flow rate during the first charging cycle for an experiment with a cutoff temperature difference of 40 K and a mean mass flow rate of 6 kg/s.

Fig. 7 presents the experimental and computational results for the first charging cycle with a mean mass flow rate of $\dot{m} = 6 \text{ kg/s}$ and a $\Delta T_{co} = 40 \text{ K}$ cutoff temperature difference, showing the temperature distribution along the position at different time steps. The entire unit is initially preheated to the cold temperature of 296 °C, except for the upper section, where some sensors register a temperature of about 450 °C. Under these conditions, the system requires 76 min to reach the cutoff temperature. The trend observed is that, at the beginning of the charging process, the top part of the unit starts to heat up uniformly, and a thermocline forms between the hot and cold regions. At approximately 3.55 m after 50 min, a sudden small decrease in temperature is observed, which coincides with the base/bottom of the upper basket, marking the beginning of a basket floor with a steel structure. Although the computational results do not capture the small temperature drop observed near the end of the charging process, they show good agreement with the experimental data throughout the rest of the domain and the different time instants. The hot temperature progression and the formation of the thermocline are well represented by the numerical model.

Fig. 8 presents the experimental and computational results for the first charging cycle with a mean mass flow rate of $\dot{m} = 6 \text{ kg/s}$ and a $\Delta T_{co} = 40 \text{ K}$ cutoff temperature difference. In this case, the unit is not initialised at the cold temperature as in the previous case. Now, the required charging time is reduced to just 61 min to reach the cutoff temperature. Although the discharging cutoff temperature difference is set to 100 K, it has no effect in this particular case since it corresponds to the initial charging cycle. Due to the initial temperature distribution, a well-defined thermocline is not observed during the first 15 min, as the first two baskets are influenced by the elevated initial temperature of the upper basket. However, from that point on, the thermocline becomes increasingly well-formed as the charging progresses. The numerical results show good agreement with the experimental data. This is the same case as in Fig. 6, but with a different initial condition. A similar temperature evolution is observed, confirming the consistency and homogeneity of the experimental results. Moreover, the small temperature drop at 3.55 m is no longer present, suggesting that it is related to the initial thermal conditions rather than a structural effect.

Fig. 9 presents the experimental and computational results for the first charging cycle with a mean mass flow rate of $\dot{m} = 2 \text{ kg/s}$ and a $\Delta T_{co} = 40 \text{ K}$ cutoff temperature difference. Although the unit is not initialised at the cold temperature, the lower mass flow rate, being three

Table 4
Thermophysical properties of the molten salt and solid filler materials.

	Solar Salt (T in $^{\circ}C$)	Clinker with MS (porosity 20 %)	KBB17/KBA4 (porosity 22 %)	Stainless steel
Density ρ [kg/m^3]	$2090 - 0.636 T$	2677	2751	7900
Specific heat capacity c_p [J/kgK]	$1443 + 0.172 T$	1125	1157	500
Absolute viscosity μ [kg/ms]	$2.27 \times 10^{-4} - 1.20 \times 10^{-4} T + 2.28 \times 10^{-7} T^2 - 1.474 \times 10^{-10} T^3$	–	–	–
Thermal conductivity λ [W/mK]	$0.443 + 1.93 \times 10^{-4} T$	1.61	1.49	15

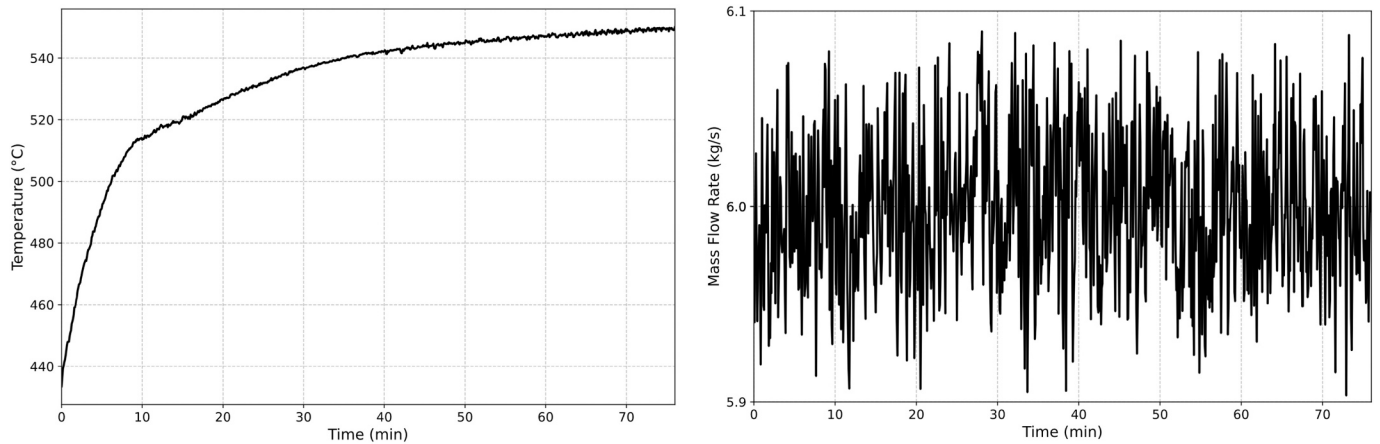


Fig. 6. Instantaneous input values for the first charging cycle: inlet temperature (left) and mass flow rate (right).

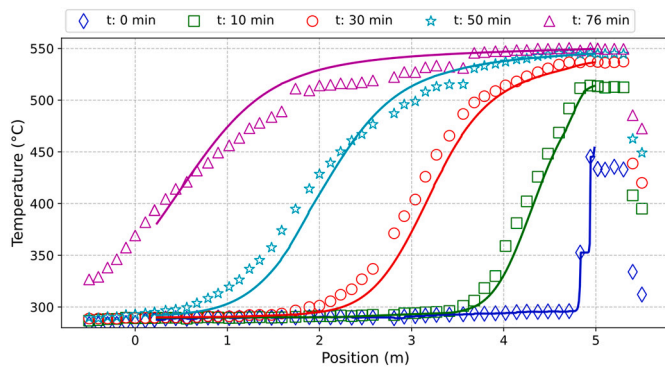


Fig. 7. Temperature distribution in the structured thermocline: simulation (solid line) vs experimental data (symbols), charging process, cold initial temperature, 6 kg/s , $\Delta T_{co} = 40 \text{ K}$.

times slower than in previous cases, results in a longer charging time. Consequently, the unit requires 125 min to reach the cutoff temperature. Despite the extended duration of the cycle and the absence of a cold start, the computational results also show good agreement with the experimental data.

4.3. Discharging tests

Fig. 10 shows the results of the first discharging cycle for a mean mass flow rate of $\dot{m} = 6 \text{ kg/s}$, and a discharging cutoff temperature difference of $\Delta T_{co} = 40 \text{ K}$. In this case, heat is rapidly extracted from the storage unit due to the high mass flow rate, resulting in a quick temperature drop in the upper part of the structure, reaching the cutoff temperature after only 40 min. A well-defined thermocline is formed, occupying nearly the entire height of the storage unit. This temperature profile moves progressively downwards in a stable manner, reflecting

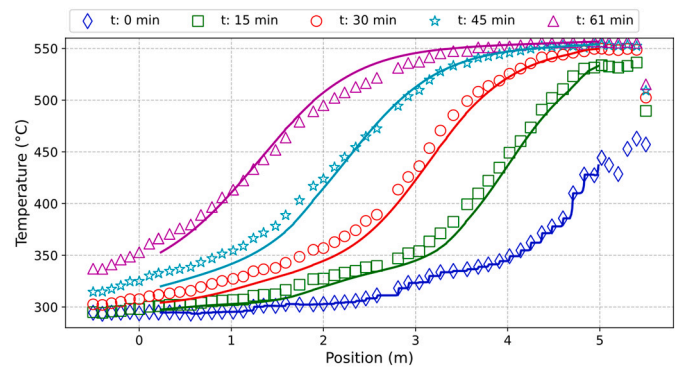


Fig. 8. Temperature distribution in the structured thermocline: simulation (solid line) vs experimental data (symbols), charging process, 6 kg/s , $\Delta T_{co} = 40 - 100 \text{ K}$.

the expected stratification behaviour during discharge. The computational results closely match the experimental data, accurately reproducing the temperature profiles throughout the process.

Fig. 11 presents the results of a discharging cycle with a mean mass flow rate of $\dot{m} = 6 \text{ kg/s}$ and a discharging cutoff temperature difference of $\Delta T_{co} = 100 \text{ K}$. In this case, the discharge time is significantly extended, not only because the unit starts fully charged (i.e., with a hot temperature profile throughout), but also due to the higher cutoff temperature, which takes longer to reach. Compared to the $\Delta T_{co} = 40 \text{ K}$ case, the thermocline becomes thinner, occupying a smaller portion of the storage unit, while the temperature profile continues to evolve in a stable and consistent manner. The computational results generally agree well with the experimental data. However, from minute 72 onwards, a slight deviation is observed, with the simulated temperature profile advancing more quickly than the experimental one. The reason for this behaviour might be caused by the lateral asymmetric outflow of the

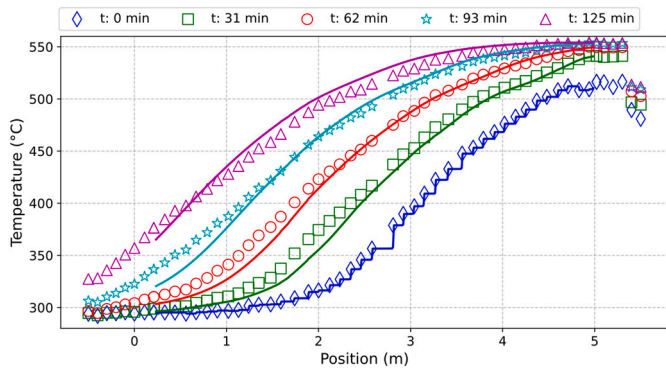


Fig. 9. Temperature distribution in the structured thermocline: simulation (solid line) vs experimental data (symbols), charging process, 2 kg/s , $\Delta T_{co} = 40 \text{ K}$.

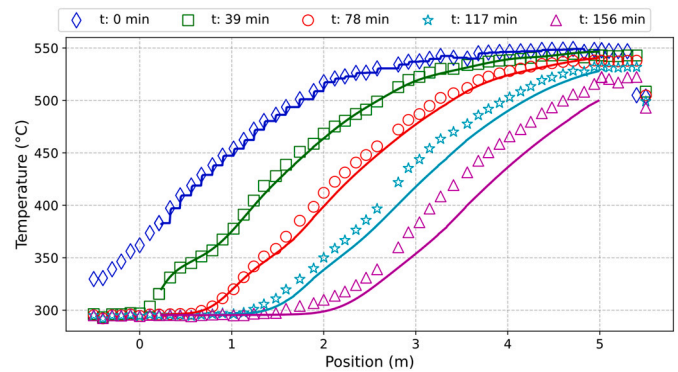


Fig. 12. Temperature distribution in the structured thermocline: simulation (solid line) vs experimental data (symbols), discharging process, 2 kg/s , $\Delta T_{co} = 40 \text{ K}$.

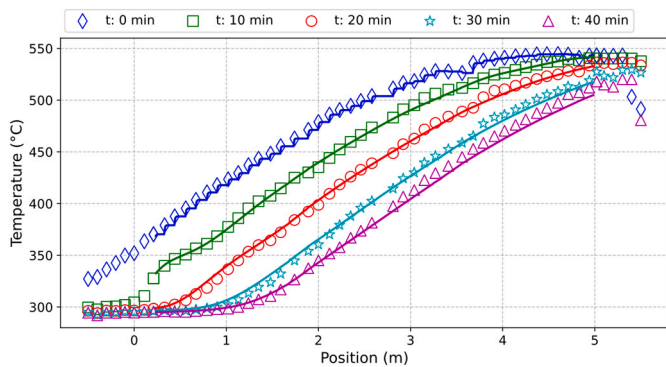


Fig. 10. Temperature distribution in the structured thermocline: simulation (solid line) vs experimental data (symbols), discharging process, 6 kg/s , $\Delta T_{co} = 40 \text{ K}$.

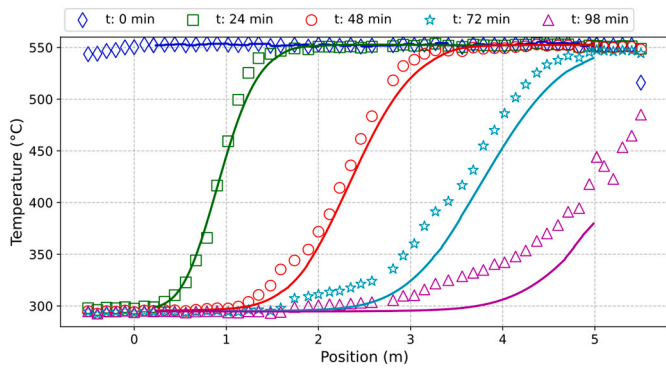


Fig. 11. Temperature distribution in the structured thermocline: simulation (solid line) vs experimental data (symbols), discharging process, 6 kg/s , $\Delta T_{co} = 100 \text{ K}$.

tank, so that the bulk flow tends toward the tank wall with the outflow. This will reduce flow speed along the centre axis, hence explaining the “faster” movement speed of the simulated curve.

Fig. 12 illustrates the first discharge cycle for a scenario previously charged using a cutoff temperature difference of $\Delta T_{co} = 40 \text{ K}$. In this scenario, the mean mass flow rate is $\dot{m} = 2 \text{ kg/s}$, resulting in a discharge duration of up to 156 min until the cutoff temperature of $520 \text{ }^\circ\text{C}$ is reached. Compared to the $\dot{m} = 6 \text{ kg/s}$ case, it is evident that the cycle with a $\dot{m} = 2 \text{ kg/s}$ exhibits a reduction in thermocline thickness, although the longer periods allow for increased thermal destratification due to conduction. Additionally, the lower cut-off temperature causes a

smaller portion of the thermocline to be extracted from the tank, allowing further growth of the thermocline thickness, compared to the $\Delta T_{co} = 100 \text{ K}$ case. The computational results generally agree well with the experimental data. However, from minute 117 onwards, a slight deviation is observed, with the simulated temperature profile advancing more quickly than the experimental one, as in the above experiment.

4.4. Cycling tests

Finally, several tests of thermal cycling were conducted. Fig. 13 shows the internal temperature profiles during the last discharge period, and after 15 cycles. A low cutoff temperature difference of $\Delta T_{co} = 40 \text{ K}$ is used. As a result, the usable storage capacity was also limited. As shown in Fig. 10, the duration of the first discharge period was approximately 40 min, which gradually decreased to around 22 min under cycling conditions. Additionally, the thermocline becomes significantly wider, spreading almost across the entire storage length. However, despite the increased thermocline thickness, the results indicate that it is possible to maintain consistent and repeatable performance after 15 full cycles, demonstrating the system’s ability to operate under long-term cycling conditions.

Fig. 14 illustrates the temperature profiles obtained during the discharge period, after 10 cycles, but with a higher cutoff temperature difference of $\Delta T_{co} = 100 \text{ K}$. During charging, a cutoff temperature difference of 40 K was kept. The duration of the discharge was 51 min, which is a significant increase. In this case, the thermocline formed during discharge appears more stable and sustainable compared to the case with a $\Delta T_{co} = 40 \text{ K}$. If a smaller thermocline thickness was desired, the cutoff temperature should be increased as much as possible. A small improvement could be achieved by reducing the mass flow rate,

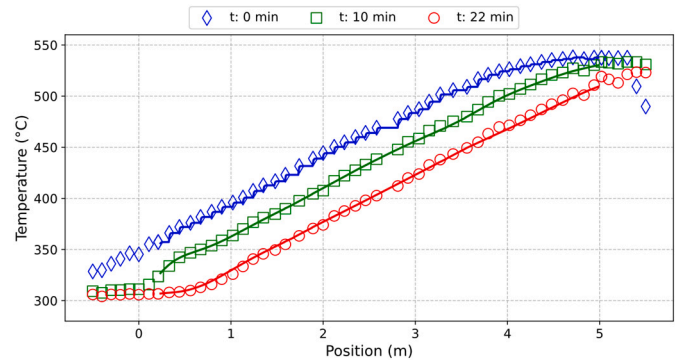


Fig. 13. Temperature distribution in the structured thermocline: simulation (solid line) vs experimental data (symbols), 15th cycle, discharging process, 6 kg/s , $\Delta T_{co} = 40 \text{ K}$.

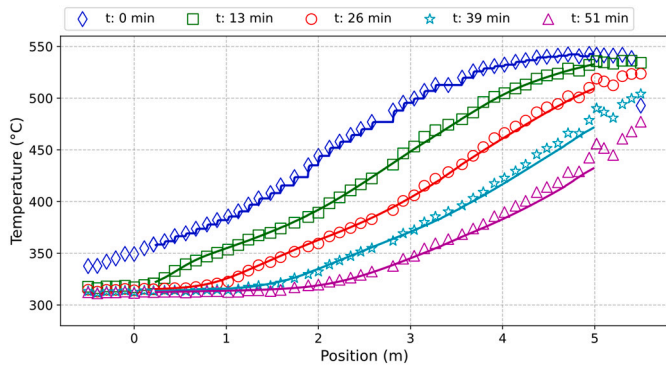


Fig. 14. Temperature distribution in the structured thermocline: simulation (solid line) vs experimental data (symbols), 10th cycle, charging process, 6 kg/s, $\Delta T_{co} = 100 K$.

allowing the fluid to spend more time in contact with the solid and improving the stratification. This highlights the importance of optimising operating conditions, such as mass flow rate and cutoff temperatures, to tailor the thermal behaviour of the system according to the specific application or performance requirements. In both cycling condition cases (using a discharging $\Delta T_{co} = 40 K$ and $\Delta T_{co} = 100 K$, respectively), the results show good agreement between experimental and computational data, with simulations initialised from the measured temperature profiles and using dynamic boundary conditions for both inlet temperature and mass flow rate.

4.5. Discharged exergy

During the discharging cycle, the exergy is evaluated to assess the efficiency and utilisation of the stored thermal energy. The discharged exergy is defined with respect to the nominal exergy of an ideal adiabatic two-tank system, in which the energy transfer occurs without heat losses to the surroundings [28]. Accordingly, the discharged exergy efficiency can be expressed as:

$$\Xi_d = \frac{\Delta E_{ST}}{\Delta E_{2T}} = \frac{\int_0^{t_d} \dot{m} \cdot [h(T_{cold}) - h(T_{out}(t)) - T_{amb} \cdot (s(T_{cold}) - s(T_{out}(t)))] dt}{\int_0^{t_d} \dot{m} \cdot [h(T_{cold}) - h(T_{hot}) - T_{amb} \cdot (s(T_{cold}) - s(T_{hot}))] dt}$$

where ΔE_{ST} and ΔE_{2T} denote the discharged exergy of the structured thermocline tank and the ideal two-tank system, respectively. The ambient temperature T_{amb} is set at 25 °C, T_{out} corresponds to the measured outlet temperature (thermocouple), T_{cold} and T_{hot} are the cold and hot temperatures, respectively, t_d the discharge time, s and h the specific entropy and enthalpy at the specified temperature, and \dot{m} the

discharged mass flow rate.

In the present analysis, the discharged exergy is evaluated for each individual discharge cycle, allowing the evolution of the system performance to be assessed over successive cycles. As shown in Fig. 15, for the case with a 40 K cutoff temperature, the discharged exergy does not reach a cyclic steady state but instead shows a continuous degradation over time. In contrast, the 100 K cutoff case rapidly stabilises into a cyclic regime. This can be attributed to the fact that in the 40 K case, the thermocline is not fully re-established between cycles and progressively degrades due to heat conduction effects, whereas in the 100 K case, the thermocline is effectively reset at each cycle. As observed earlier, the thermocline in the last cycle of the 100 K case is significantly narrower than in the 40 K case.

In addition to the cutoff effect, the charging temperature also plays a role in the observed discharged exergy values. Although a set point of 560 °C was defined for the exergy calculation, this value was not achieved in practice. In both cutoff cases, the average charging inlet temperature during the first cycle is approximately 555 °C, and it progressively decreases to around 545 °C in the subsequent cycles. This gradual reduction in charging temperature partially explains the lower discharged exergy values observed, as the effective temperature difference available for charging and discharging decreases over time.

5. Conclusions

This work presented the first pilot-scale implementation of a structured thermocline thermal energy storage (TES) system, combining experimental validation with numerical modelling to assess its feasibility under realistic operating conditions. The storage concept, based on vertically stacked baskets filled with refractory bricks and integrated into the TESIS facility, demonstrated robust and repeatable thermal stratification during multiple charging and discharging cycles. A one-dimensional unsteady numerical model was developed and validated against experimental data across a range of scenarios, including different mass flow rates, initial conditions, and cutoff temperatures. The model showed excellent predictive capability in capturing the thermocline formation, evolution, and overall system dynamics.

During charging tests, results confirmed that the thermocline formed consistently across various operating conditions. Two charging cases with a mean mass flow rate of 6 kg/s ($\dot{m} = 6 \text{ kg/s}$) were analysed: one with fully cold initial conditions, and another with a partially preheated temperature profile in the upper region of the tank (from 3 to 5 m). In both cases, the charging cutoff temperature difference was set to 40 K ($\Delta T_{co} = 40 K$). Although the second case used a $\Delta T_{co} = 100 K$ for the subsequent discharge phase, the charging conditions remained identical. The fully cold case required 76 min to reach the cutoff temperature, while the partially preheated case reduced the charging time to 61 min.

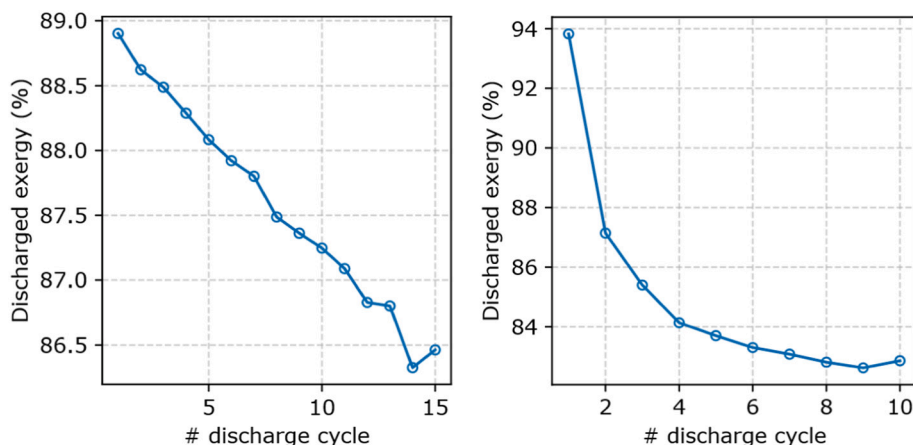


Fig. 15. Discharged exergy for a cutoff temperature of 40 K (left) and 100 K (right) with a mass flow rate of 6 kg/s.

Although the heat-up was faster in the latter, the presence of a higher initial temperature led to delayed stratification in the early stages, as the thermocline formation was initially influenced by the existing gradient. At a lower mean mass flow rate of $\dot{m} = 2 \text{ kg/s}$, the charging process extended to 125 min, yet thermal stratification was still successfully established.

Discharging tests were carried out for two cutoff conditions ($\Delta T_{co} = 40 \text{ K}$ and $\Delta T_{co} = 100 \text{ K}$) using a $\dot{m} = 6 \text{ kg/s}$. In the $\Delta T_{co} = 40 \text{ K}$ case, the system did not begin fully charged and reached the cutoff temperature after 40 min. A broad thermocline formed, extending across most of the tank's height, and the temperature profile evolved in a stable manner. In contrast, the $\Delta T_{co} = 100 \text{ K}$ case started from a fully charged state and discharged over 98 min. Despite the longer duration, a much thinner thermocline was maintained throughout the process, with a similarly stable and consistent temperature evolution. At a lower $\dot{m} = 2 \text{ kg/s}$, the discharge cycle extended to 156 min. This case, using a $\Delta T_{co} = 40 \text{ K}$ and an initial condition not fully hot but comparable in shape to the $\dot{m} = 6 \text{ kg/s}$ case, exhibited a slightly thinner thermocline that did not span the full height of the structure. These observations confirm the influence of both mass flow rate and cutoff temperature on the thermocline thickness and discharge duration.

Thermal cycling tests confirmed the long-term stability and repeatability of the system. In the $\Delta T_{co} = 40 \text{ K}$ discharge case, a gradual reduction in discharge duration and broadening of the thermocline were observed after repeated cycling. When a $\Delta T_{co} = 100 \text{ K}$ was applied during discharge, the thermocline at cycle 10 was significantly narrower than in the $\Delta T_{co} = 40 \text{ K}$ case, indicating improved stratification. However, the discharge duration was reduced from 98 min in the first cycle to 51 min in the eleventh. The observed widening of the thermocline over successive thermal cycles appears to be primarily driven by thermal conduction. Additionally, the discharge cutoff temperature plays a major role in preserving or resetting the thermocline: higher cutoffs allow the system to restart from a sharper stratification state, while lower cutoffs extract only part of the thermocline, allowing the remaining gradient to persist and further broaden due to conduction. Finally, although the mass flow rate also influences thermocline thickness, with lower flow rates generally leading to improved stratification, its impact is less significant than that of the cutoff temperature. Regarding discharged exergy, the 100 K cutoff case exhibits a cyclic steady behaviour, whereas the 40 K case does not, showing instead a progressive degradation over time, which can be attributed to the reset of the thermocline thickness and to conduction effects.

From a practical perspective, a higher cutoff temperature generally enables a more efficient utilisation of the stored thermal energy. However, in the context of concentrated solar power (CSP) systems, one must carefully consider the characteristics and limitations of the attached process. The steam cycle, in particular, must be capable of tolerating a more pronounced decrease in discharge temperature, which may pose operational challenges. Moreover, any increase in the outlet temperature during the charging phase must be managed by the solar field, for instance by adjusting the mass flow rate or through partial defocusing of the mirrors. An alternative operational approach could involve discharging the storage system only until the outlet temperature begins to decline, then pausing until the following day to continue discharging and utilising the recovered heat for preheating purposes. While this strategy could offer benefits in terms of efficiency and flexibility, it would also introduce additional complexity and therefore requires further investigation.

Overall, the findings validate the structured thermocline TES concept as a scalable and effective solution for high-temperature energy storage. The good agreement between experimental and numerical results confirms the suitability of the proposed 1D model for predictive simulation, design, and integration into larger-scale energy systems and control frameworks.

Nomenclature

Symbols		
a_s	specific surface area	(m^2/m^3)
c_p	specific heat capacity	(J/kgK)
d_{channel}	channel diameter	(m)
D	storage diameter	(m)
E	discharged exergy from storage	(J)
h	specific enthalpy	(J/kg)
h_{bed}	storage height	(m)
\dot{m}	mass flow rate	(kg/s)
N	number of nodes	(–)
N_{it}	number of channels	(–)
Nu	Nusselt number, $ad_{\text{channel}}/\lambda_f$	(–)
\dot{q}_{loss}	volumetric heat losses	(W/m^3)
s	specific entropy	(J/kgK)
t	time	(s)
T	temperature	($^{\circ}\text{C}$)
v_f	fluid flow velocity	(m/s)
z	axial coordinate	(m)
Greek symbols		
$\hat{\alpha}$	volumetric heat transfer coefficient	($\text{W/m}^3\text{K}$)
α	superficial heat transfer coefficient	($\text{W/m}^2\text{K}$)
Δ	difference	(–)
ϵ	void fraction	(–)
λ	thermal conductivity	(W/mK)
μ	dynamic viscosity	(Pa s)
ρ	density	(kg/m^3)
Ξ	discharged exergy efficiency	(–)
Subscripts		
amb	Ambient	
c	Charge	
co	Cutoff Temperature Difference	
d	Discharge	
f	Fluid	
hyd	Hydraulic	
i	Node I	
i-	Previous Node	
i+	Following Node	
s	Solid	
Superscripts		
0	Previous Time Step	
Abbreviations		
2T	Two Tank	
CV	Control Volume	
CSP	Concentrated Solar Power	
FVM	Finite Volume Method	
HTF	Heat Transfer Fluid	
PB	Packed Bed	
PCM	Phase Change Material	
ST	Structured	
TDMA	Tri-Diagonal Matrix Algorithm	
TES	Thermal Energy Storage	
UDS	Upwind Differential Scheme	

CRediT authorship contribution statement

Jordi Vera: Writing – review & editing, Supervision, Software, Methodology, Formal analysis, Conceptualization. **Christian Odenthal:** Writing – review & editing, Writing – original draft, Supervision, Resources, Project administration, Methodology, Investigation, Funding acquisition, Data curation, Conceptualization. **Oriol Sanmartí:** Writing – review & editing, Writing – original draft, Visualization, Validation, Software, Investigation, Formal analysis, Data curation. **Carlos D. Pérez-Segarra:** Writing – review & editing, Writing – original draft, Supervision, Resources, Project administration, Funding acquisition, Conceptualization.

Declaration of competing interest

The authors declare that they have no known competing financial interests or personal relationships that could have appeared to influence the work reported in this paper.

Acknowledgements

This work is carried out in the framework of the Newline project. It is supported under the umbrella of CSP-ERA.NET 1st Cofund Joint Call and by the following National Agencies: AEI (Spain), CDTI (Spain), Jülich (Germany), and SFOE (Switzerland). CSP-ERA.NET is supported by the European Commission within the EU Framework Programme for Research and Innovation Horizon 2020 (Cofund ERA-NET Action, N° 838311).

Oriol Sanmartí acknowledges the financial support from the “Departament de Recerca i Universitats de la Generalitat de Catalunya” and the “Fons Social Europeu” with the predoctoral grant JOAN ORÓ FI AGAUR (2023 FI 00192).

Data availability

Data will be made available on request.

References

- [1] A. Gil, M. Medrano, I. Martorell, A. Lázaro, P. Dolado, B. Zalba, L.F. Cabeza, State of the art on high temperature thermal energy storage for power generation. Part 1—Concepts, materials and modellization, *Renew. Sust. Energy. Rev.* 14 (2010) 31–55, <https://doi.org/10.1016/j.rser.2009.07.035>.
- [2] H.M. Ali, T. Rehman, M. Arıcı, Z. Said, B. Duraković, H.I. Mohammed, R. Kumar, M.K. Rathod, O. Buyukdagli, M. Teggur, *Advances in thermal energy storage: Fundamentals and applications*, *Prog. Energy Combust. Sci.* 100 (2024) 101109, <https://doi.org/10.1016/j.pecs.2023.101109>.
- [3] M. Mubarrat, M.M. Mashfy, T. Farhan, M.M. Ehsan, Research advancement and potential prospects of thermal energy storage in concentrated solar power application, *Int. J. Thermofluids* 20 (2023) 100431, <https://doi.org/10.1016/j.ijft.2023.100431>.
- [4] R. Jacob, S. Riahi, M. Liu, M. Belusko, F. Bruno, Technoeconomic impacts of storage system design on the viability of concentrated solar power plants, *J Energy Storage* 34 (2021) 101987, <https://doi.org/10.1016/j.est.2020.101987>.
- [5] G. Alva, Y. Lin, G. Fang, An overview of thermal energy storage systems, *Energy* 144 (2018) 341–378, <https://doi.org/10.1016/j.energy.2017.12.037>.
- [6] X. He, J. Qiu, W. Wang, Y. Hou, M. Ayyub, Y. Shuai, A review on numerical simulation, optimization design and applications of packed-bed latent thermal energy storage system with spherical capsules, *J Energy Storage* 51 (2022) 104555, <https://doi.org/10.1016/j.est.2022.104555>.
- [7] A. Gautam, R.P. Saini, A review on technical, applications and economic aspect of packed bed solar thermal energy storage system, *J Energy Storage* 27 (2020) 101046, <https://doi.org/10.1016/j.est.2019.101046>.
- [8] T. Chekifi, M. Boukraa, Thermocline storage for concentrated solar power plants: Descriptive review and critical analysis, *J Energy Storage* 55 (2022) 105773, <https://doi.org/10.1016/j.est.2022.105773>.
- [9] M.N. Strasser, R.P. Selvam, A cost and performance comparison of packed bed and structured thermocline thermal energy storage systems, *Sol. Energy* 108 (2014) 390–402, <https://doi.org/10.1016/j.solener.2014.07.023>.
- [10] O. Sanmartí, J. Vera, S. Torras, C.D. Pérez-Segarra, Parametric study for a structured thermal energy storage system for concentrated solar power plants, *Energy* (2024) 132271, <https://doi.org/10.1016/j.energy.2024.132271>.
- [11] O. Sanmartí, J. Vera, S. Torras, C.D. Pérez-Segarra, Numerical study of encapsulated phase change material integration in structured thermal energy storage systems for concentrated solar power, *Res. Eng. Des.* 28 (2025) 107263, <https://doi.org/10.1016/j.rineng.2025.107263>.
- [12] J.E. Pacheco, S.K. Showalter, W.J. Kolb, Development of a molten-salt thermocline thermal storage system for parabolic trough plants, *J. Sol. Energy Eng.* 124 (2002) 153–159, <https://doi.org/10.1115/1.1464123>.
- [13] J.-F. Hoffmann, T. Fasquelle, V. Goetz, X. Py, A thermocline thermal energy storage system with filler materials for concentrated solar power plants: Experimental data and numerical model sensitivity to different experimental tank scales, *Appl. Therm. Eng.* 100 (2016) 753–761, <https://doi.org/10.1016/j.applthermaleng.2016.01.110>.
- [14] M.A. Keilany, S. Vannerem, M. Milhê, Q. Falcoz, J.-J. Bézian, G. Flamant, Experimental and numerical study of combining encapsulated phase change material to sensible heat storage material in one-tank pilot scale thermal energy storage, *J Energy Storage* 51 (2022) 104504, <https://doi.org/10.1016/j.est.2022.104504>.
- [15] G. Zanganeh, A. Pedretti, S. Zavattoni, M. Barbato, A. Steinfeld, Packed-bed thermal storage for concentrated solar power – Pilot-scale demonstration and industrial-scale design, *Sol. Energy* 86 (2012) 3084–3098, <https://doi.org/10.1016/j.solener.2012.07.019>.
- [16] G. Zanganeh, R. Khanna, C. Walser, A. Pedretti, A. Haselbacher, A. Steinfeld, Experimental and numerical investigation of combined sensible–latent heat for thermal energy storage at 575°C and above, *Sol. Energy* 114 (2015) 77–90, <https://doi.org/10.1016/j.solener.2015.01.022>.
- [17] S. Advait, D.R. Parida, K.T. Aswathi, N. Dani, U.K. Chetia, K. Chattopadhyay, S. Basu, Experimental investigation on single-medium stratified thermal energy storage system, *Renew. Energy* 164 (2021) 146–155, <https://doi.org/10.1016/j.renene.2020.09.092>.
- [18] N. Stathopoulos, N. Papadimitriou, V. Belessiotis, E. Papanicolaou, Packed bed thermocline thermal energy storage for medium-temperature concentrating solar systems: Numerical and experimental study, *J. Power Energy Eng.* 11 (2023) 1–23, <https://doi.org/10.4236/jpee.2023.115001>.
- [19] A. Bruch, J.F. Fourmigué, R. Couturier, Experimental and numerical investigation of a pilot-scale thermal oil packed bed thermal storage system for CSP power plant, *Sol. Energy* 105 (2014) 116–125, <https://doi.org/10.1016/j.solener.2014.03.019>.
- [20] C. McGregor, L.C. Snyman, Design and Performance Testing of a Structured Packing for Thermal Energy Storage Applications, Begel House Inc., in, 2023, <https://doi.org/10.1615/IHTC17.430-170>.
- [21] J. Coventry, J.F. Torres, Z. Kee, M.V. Bozorg, M. Taheri, A. Mojiri, J. Pye, S. Bell, G. Will, T. Steinberg, Development of a Packed Bed Thermal Energy Storage Prototype with Sodium as the Heat Transfer Fluid, (n.d.).
- [22] S. Zunft, M. Hänel, M. Krüger, V. Dreißigacker, F. Göhring, E. Wahl, Jülich solar power tower—Experimental evaluation of the storage subsystem and performance calculation, *J. Sol. Energy Eng.* 133 (2011), <https://doi.org/10.1115/1.4004358>.
- [23] C. Odenthal, J. Tombrink, F. Klasing, T. Bauer, Comparative study of models for packed bed molten salt storage systems, *Appl. Therm. Eng.* 226 (2023) 120245, <https://doi.org/10.1016/j.applthermaleng.2023.120245>.
- [24] B. Xie, N. Baudin, J. Soto, Y. Fan, L. Luo, Wall impact on efficiency of packed-bed thermocline thermal energy storage system, *Energy* 247 (2022) 123503, <https://doi.org/10.1016/j.energy.2022.123503>.
- [25] J. Vera, O. Sanmartí, S. Torras, C.D. Pérez-Segarra, Optimizing structured thermocline performance using a 3D+1D advanced model, *Energy Convers. Manag.* X 28 (2025) 101252, <https://doi.org/10.1016/j.ecmx.2025.101252>.
- [26] C. Odenthal, F. Klasing, P. Knödler, S. Zunft, T. Bauer, Experimental and Numerical Investigation of a 4 MWh High Temperature Molten Salt Thermocline Storage System with Filler, Daegu, South Korea, 2020, p. 190025, <https://doi.org/10.1063/5.0028494>.
- [27] A.B. Zavoico, Solar Power Tower Design Basis Document, Revision 0, Sandia National Lab. (SNL-NM), Albuquerque, NM (United States); Sandia National Lab. (SNL-CA), Livermore, CA (United States), 2001, <https://doi.org/10.2172/786629>.
- [28] C. Odenthal, F. Klasing, T. Bauer, Parametric study of the thermocline filler concept based on exergy, *J Energy Storage* 17 (2018) 56–62, <https://doi.org/10.1016/j.est.2018.01.009>.